small structures
www.small-structures.com

Conversion of Renewable Lignocellulosic Biomass-Derived Nanocellulose into Graphene via Pyrolysis and High Shear-Mediated Exfoliation

*Yu Matsueda, Colin L. Raston, and Elsa Antunes**

Graphene is extensively researched due to its diverse range of applications and remarkable properties. Current production methods such as sonication and chemical vapor deposition (CVD) are energy-intensive and unsustainable, restricting its industrial use. The vortex fluidic device (VFD) is a thin film processing platform that rapidly spins a tube to generate high shear forces and offers a low-cost and sustainable method for graphene production. However, previous studies on exfoliation are limited to utilizing graphite as the feed, which not only is unsustainable but also generates high carbon emissions due to mining processes. In this study, nanocellulose crystal (NCC), a sustainable material derived from lignocellulosic biomass, is used as the precursor for graphene production. The NCCs are first pyrolyzed at 500–800 °C at 5 °C min^{-1} for 60 min and then converted to graphene in the VFD using only water as the solvent. The biochar properties significantly impact the exfoliation degree, and 600 °C is the optimal pyrolysis temperature. The Earth's magnetic field and rotation direction also affect the VFD processing. The graphene shows a relatively high quality with an I_D/I_G ratio of 0.60, an I_{2D}/I_G ratio of 0.15, and transmission electron microscopy confirming <6 layers. This process offers a sustainable route for graphene synthesis using renewable biomass feedstock.

1. Introduction

Graphene is one of the most revolutionary materials discovered in the twenty-first century and has been widely studied due to its immense range of applications, with a projected global market value in 2025 of over AUD$ 800 million.[1] It is a crystalline, 2D monolayer carbon material composed of sp^2 hybridized carbon that form a hexagonal honeycomb lattice structure. Its unique properties such as its high mechanical strength (Young's modulus and tensile strength equal to 1 TPa and 125 GPa respectively), thermal conductivity (5000 W m^2 K), electrical conductivity, and specific surface area (SSA) (2630 m^2 g^{-1}) make it highly valuable and applicable in many fields.[2] A major limitation of graphene, however, is its current production method, which are costly, unscalable, and unsustainable, resulting in high commercial prices (USD$ 67 to 200 per kg) and prohibiting their use in many industrial sectors.[3,4] As such, there is a large emphasis on finding a scalable, low-cost method that utilizes renewable sources for graphene synthesis.

Graphene can be produced through either top-down or bottom-up methods. Top-down methods include ball milling, sonication, fluid exfoliation, and chemical exfoliation, typically using graphite as the precursor and obtaining graphene via layer separation. Bottom-up methods include chemical vapor deposition (CVD), epitaxial growth, and pyrolysis and use carbon precursors such as methane or biomass as building blocks to form graphene.[1] **Table 1** compares the processing conditions, scalability, and quality of graphene obtained from the different production methods. Although CVD and sonication are commonly used, they suffer from low production rates and limited scalability. Sonication has been reported to achieve a maximum production rate of 1 g h^{-1} with little possibility of scale-up,[5,6] while CVD is an energy intensive process (>900 °C) that requires the use of metal catalysts and is unrealistic for large scale processes.[7,8] Ball milling results in defective graphene due to high impact collisions along with contamination from degradation of the balls, while chemical exfoliation uses toxic chemicals such as sulfuric acid (H_2SO_4) and potassium permanganate ($KMnO_4$).[9,10]

Fluid exfoliation has recently been seen as a promising method for graphene synthesis due to its low cost, scalability, and minimal use of chemicals. It utilizes high shear rates (minimum 10^4/s) to overcome the dispersion forces in graphitic materials to generate 2D graphene layers.[6] Paton et al.[11] first used a commercial rotor-stator mixer to

Y. Matsueda, E. Antunes
College of Science and Engineering
James Cook University
Townsville 4814, Australia
E-mail: elsa.antunes1@jcu.edu.au

C. L. Raston
Flinders Institute for Nanoscale Science and Technology
College of Science and Engineering
Flinders University
Adelaide 5042, Australia

The ORCID identification number(s) for the author(s) of this article can be found under https://doi.org/10.1002/sstr.202500532.

DOI: 10.1002/sstr.202500532

Table 1. Comparison of process conditions, production rate, and scalability of current graphene production methods.

Method	Typical feed	Process conditions and energy costs	High-quality graphene	Scalable	Comments	Refs.
Bottom-up						
Epitaxial growth	Silicon carbide	1500 °C high vacuum	✓	✗	High temperature limits sustainability	[1]
CVD	H_2, CH_4	600–1600 °C <240 min Requires H_2 Fe, Ni, or Cu catalyst <34 MJ kg^{-1} graphene	✓	✗	High energy and H_2 consumption, difficult to scale to industry	[66–68]
Pyrolysis	Biomass	450–1200 °C 0.5–6 h Acid or metal catalyst	✗	✓	Removal of catalyst from graphene requires strong acids	[8,69]
Laser-induced	Plastics, biomass	CO_2 laser Power: 0.1–2 W Scan rate: 20–500 mm s^{-1}	✓	✗	Thin films and low scan rates make scaling challenging	[70]
Top-down						
Sonication	Graphite, biochar	25 °C 0.5–15 h 80–600 W Solvents: water, ethanol, acetone <309 MJ kg^{-1} graphene	✗	✗	Independent of volume making scalability difficult	[5,68,69]
Chemical exfoliation	Graphite, biochar	25–100 °C 4–24 h $KMnO_4$, H_2SO_4, $NaNO_3$ 35 810 MJ.kg graphene	✗	✓	Releases harmful pollutants	[1,10,68]
Fluid exfoliation	Graphite	25 °C 2000-18 000 rpm 0.5–8 h 1–3 mg graphite ml^{-1} Solvent: water, N,N-dimethylformamide (DMF)	✓	✓	Challenges include low yield and graphene concentrations	[9,18,71,72]
Ball milling	Graphite	150–1200 rpm 1–60 h Exfoliating agent: melamine, metals >52 900 MJ kg^{-1} graphene	✗	✓	Often paired with sonication to increase exfoliation	[9,68,71]

exfoliate graphite into few-layer graphene and achieved a production rate of 5.3 g h^{-1}, significantly higher than sonication (<0.1 g h^{-1}) and ball milling (1 g h^{-1}).[12] However, a limitation with their experiment was that exfoliation was only localized at the gap (<100 microns) between the rotor and stator, limiting its potential to scale. For this reason, Karagiannidis et al.[13] instead used a microfluidizer to force the liquid through a small channel (diameter = 100 microns), with a major advantage over rotor-mixing being that high shear rate is applied to the whole volume. They were able to exfoliate graphite into low-defect graphene flakes (1–5 microns lateral size and 19 nm average thickness). Another study also showed that graphene flakes could be obtained by pumping a graphite solution at 5 MPa through a narrow tube (2 mm inner diameter) to generate high shear rates (10^5 s^{-1}) and that the process could be easily scaled by simply increasing the number of tubes.[14] However, the small tube diameters used in these experiments mean that these devices are prone to clogging and are restricted to low graphite concentrations.

The vortex fluidic device (VFD) is a low-cost, scalable device that rapidly rotates a tube (up to 9000 rpm) at an angle (0°–90°) to form a thin film of liquid (≥ ≈0.22–micron thickness) at the tube surface.[15] The device typically houses a small quartz or borosilicate glass tube (17.5 mm internal diameter and 185 mm length), but larger VFDs are also available (46 mm internal diameter and 450 mm length) and can be configured to "continuous mode" for constant production, highlighting the scalability of the process.[16] Chen et al.[17] used this device to exfoliate graphite into graphene sheets (2–10 layers) and found a tilt angle of 45° at 7000 rpm for 30 min in N-methyl-pyrrolidone (NMP) solvent to be optimal. Wahid et al.[18] further showed that under the same conditions, water can instead be used as the solvent and obtained graphene (> 5 layers), with Raman spectra confirming a minimal degree of defects. Though these studies (and other exfoliation papers) highlight the potential for fluid exfoliation to achieve low-defect graphene at high production rates, they are limited to utilizing graphite as the precursor, which is not only nonrenewable but also contributes ≈5.3 tonnes $CO_{2\text{-eq}}$ per tonne graphite due to mining processes.[19] Therefore,

an alternative feedstock is crucial for sustainable graphene synthesis.

Biochar is a carbon-rich solid that has potential to be a renewable precursor for graphene production. It is produced through the pyrolysis of dry biomass (10–15 wt% moisture), a process that occurs at temperatures above 300 °C in oxygen free atmospheres.[20] During pyrolysis, the volatile elements of the biomass (typically hydrogen and oxygen compounds) are removed as gases or vapor, leaving a biochar primarily composed of carbon (60–95 wt%).[21] However, due to the disordered nature of biomass, the structure of the resulting material is typically amorphous as opposed to the crystalline nature of graphene. A catalyst can be added to assist with the formation of crystalline graphene, as demonstrated by You et al.[22] who pyrolyzed wood chips at 700–1200 °C for 1 h with an Fe catalyst to form graphitic layers via dissolution-precipitation. After Fe removal, the biomass-derived graphite was exfoliated using a horn-sonicator at 10 300 rpm to form few-layered graphene (4.1 nm thickness). Chen et al.[7] used hydrothermal treatment at 150 °C to first dissolve the lignin and hemicellulose fractions of wheat straw before pyrolyzing the cellulose fraction at 2600 °C. They observed that the cellulose itself was a layered structure, which was then exfoliated (using KOH catalyst) and directly converted into graphene during pyrolysis. The analysis showed that the resulting material was composed of 2–10 layered graphene with minimal defects and a high degree of graphitization (90.7%). Although the extreme temperature (2600 °C) used in their study raises issues with regard to energy usage and sustainability, it highlighted how the ordered structure of cellulose favored the production of high-quality graphene.

Nanocellulose crystals (NCC) are a highly crystalline nanomaterial derived from lignocellulosic biomass which is separated from the cellulose fraction. This is achieved using chemicals to remove the lignin and hemicellulose fractions, resulting in a relatively pure cellulose component (approximately only <1 wt% lignin remaining).[23] The cellulose then undergoes an acid hydrolysis step to form NCC. Many experiments have shown that during cellulose pyrolysis, condensed aromatic structures (similar to the molecular structure of graphene) in the biochar are present at temperatures between 500 and 800 °C[24–26] indicating the potential to convert NCC into graphitic layers at relatively low temperatures, which, when combined with fluid exfoliation, offers a low-energy route to graphene production with sustainable feedstock and eco-friendly solvent without the need for catalysts.

This work investigates the synthesis of graphene under slow pyrolysis (500–800 °C) using wood-derived nanocellulose as the starting material. To the authors knowledge, this is the first study to investigate the production of biochar-derived graphene under mild pyrolysis conditions (<900 °C) without the use of external chemicals or catalysts. The NCC-derived biochar was characterized, and the material was dispersed in water and processed in the VFD to obtain graphene. The biochar properties (SSA, morphology, and functional groups) were shown to greatly impact the transformation of the biochar followed by exfoliation, with the VFD conditions optimized to maximize graphene production. This approach shows great promise to be a low-cost, sustainable, and catalyst-free method to synthesize graphene using a lignocellulosic biomass-derived feedstock.

2. Experimental Section

The overall methodology for this study is summarized in **Figure 1** and consists of three stages; 1) pyrolysis of nanocellulose to obtain biochar, 2) the transformation of biochar in graphene followed by in situ exfoliation in the VFD, and 3) characterization of the product before and after graphene formation. Commercial sodium-stabilized sulfonated NCCs were purchased from Celluforce, Canada (CAS 9004-34-6), and used in this work. The crystallinity index of the NCCs was calculated using the Segal equation[27] and determined by X-ray diffraction (XRD) to be 72% (Figure S1, Supporting Information).

2.1. Nanocellulose Pyrolysis

Nanocellulose pyrolysis was conducted in a vertical tube furnace (VTF 120 °C 1 Zone model, Figure S2, Supporting Information). The quartz tube (600 mm length and 50 mm outer diameter) was loaded in a temperature-programmed tube furnace and insulated with thermal ceramic blocks (1500 grade alumina fiber). At the beginning of each experiment, 9.0 g of NCCs was placed in a preweighed cylindrical quartz vessel (80 mm length and 35 mm outer diameter) and placed inside the quartz tube. The reactor was then purged with N_2 (99.9% purity) for 30 min to remove any air inside the furnace. The NCC was pyrolyzed at 500, 600, 700, and 800 °C at 5.0 °C min^{-1} with a holding time of 60 min at the maximum temperature and an N_2 flowrate of 50.0 mL min^{-1}. Previous studies on cellulose pyrolysis have shown that low heating rates (<6 °C min^{-1}) favor biochar yields, which is desirable for an economically sustainable process.[28] The yield of the biochar was calculated using Equation (1).

$$\text{Biochar yield (wt\%)} = \frac{m_{final}}{m_{initial}} \times 100\% \quad (1)$$

where m_{final} is the solid residue after pyrolysis, and $m_{initial}$ is the initial mass of NCC. Each experiment was conducted in triplicates, and the carbonized NCCs were labelled as CNCC-X, where X denotes the maximum pyrolysis temperature.

2.2. Characterization

A Fourier transform infrared (FT-IR) spectrometer (IRSpirit-T, Shimadzu, Japan) was used to determine the surface functional groups present in the NCC and CNCC samples using a resolution of 4 cm^{-1}, wavenumber of 450–4000 cm^{-1}, and 20 scans per spectrum. XRD (Bruker D2 Phaser) was used to determine the crystal structure of the NCC and CNCC samples using a copper anode with wavelength 1.54060 Å, operating at 30 kV and 10 mA. Raman spectroscopy was conducted on the NCC, CNCC, and graphene (referred to as G-CNCC) samples using an Alpha300RAS Raman microscope (Witec, Ulm, Germany) with an excitation wavelength of 532 nm at 1 mW power. The OriginPro 2025 software was used for peak deconvolution following the methodology described by Smith et al.[29]

The thermal stability of the raw NCC was determined by using a thermogravimetric analyzer (NETZSCH STA 449F3, Germany). A mass of 12.4 mg was placed into an alumina crucible and heated from 30 °C to 1000 °C at a heating rate of

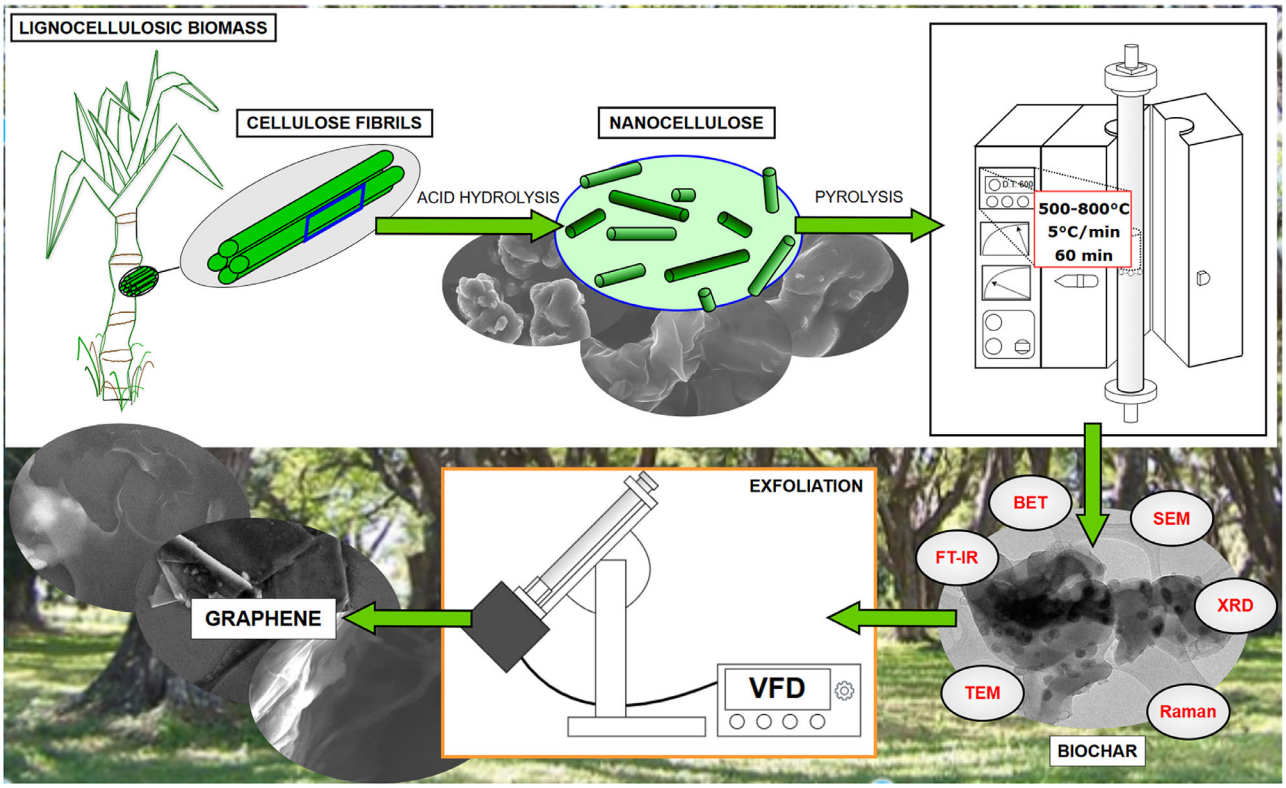

Figure 1. A summary of the methodology for this study, where the wood-derived nanocellulose was purchased directly from Celluforce and only shown here to illustrate the origin of the feedstock. The nanocellulose was pyrolyzed at 500–800 °C (with 600 °C being optimal for graphene production) at 5 °C min^{-1} for 60 mins under a flowrate of 50 mL N_2 min^{-1} and transformed into graphene in the VFD.

10.0 °C min^{-1} under a nitrogen flow rate of 50.0 mL min^{-1}. The elemental analysis (CHNSO) of the biochar was conducted using an elemental analyzer (Thermo FlashSmart elemental analyzer). In each trial, 3.0 mg of sample was combusted, and the resulting gases were analyzed. Each sample was analyzed in triplicates, and the final composition was averaged.

The SSA of the biochar samples was analyzed according to the Brunauer–Emmett–Teller (BET) nitrogen adsorption method, and the single point method was used to determine the total pore volume. The pore size distribution was analyzed using the density functional theory (DFT) method as it is more suited than other methods such as the Barrett–Joyner–Halenda (BJH) for micropore analysis.[30]

Scanning electron microscopy (SEM) was conducted on the raw NCCs, CNCC, and its graphene derivative (G-CNCC). The NCC powder was mounted on conductive carbon tapes (attached to aluminum pin stubs), coated with 15 nm thickness of carbon, and analyzed at an accelerating voltage of 10 kV using a Hitachi SU7000 Field Emission Scanning Electron Microscope. The CNCC was dispersed in milli-q water, sonicated for 20 min, drop mounted onto a silicon wafer (attached to carbon adhesive tape and aluminum pin stub), and analyzed using a Hitachi SU5000 SEM machine at an accelerating voltage of 5 kV. Atomic force microscopy (AFM) was also conducted on the drop-casted G-CNCC at the optimal VFD conditions. The measurements were performed using a Bruker Icon PT AFM in tapping mode at a peak force of 200 pN. Transmission electron microscopy (TEM) was also conducted on the CNCC and G-CNCC. The samples were first dispersed in 100% ethanol, sonicated for 5 min, drop mounted on lacey carbon-formvar coated copper grids, and analyzed using a JEOL 2100 TEM at 200 kV.

UV-VIS spectroscopy (Shimadzu UV2600) was conducted on the final graphene solution (using quartz cuvettes with an optical path of 10 mm in distilled water) obtained at optimal conditions to estimate the graphene yield. The final concentration (c) was determined using Beer–Lambert's law (Equation (2)):

$$A = \varepsilon c L \tag{2}$$

where A is equal to the absorbance at 660 nm, ε is equal to the absorbance coefficient and was averaged from a range of values in a previous study to be 1534.5 (mL mg^{-1} m^{-1}), and L is equal to the optical path length (m).[31]

2.3. Biochar Conversion to Graphene

The transformation of CNCC into graphene (G-CNCC) was conducted using the VFD (Figure S3, Supporting Information). For each experiment, the biochar solution (1.0 mg CNCC/mL milli-q water) was sonicated for 15 min before 1.0 mL of solution was placed into the VFD tube. The tube opening was then covered in parafilm, and the processing parameters of the instrument were systematically explored: the rotational speed of the tube

(5000–8500 revolutions per minute (RPM)), rotation direction (clockwise or counterclockwise relative to looking out of the tube), residence time (RT) (15–240 min), and the orientation of the tube relative to the Earth's magnetic field (N, E, S, or W). The tilt angle was maintained at 45° as it is reported to be optimal for most VFD applications.[15] The resulting solution was diluted using milli-q water by a factor of 10 and allowed to settle for 20 min before directly drop casting the top layer (Figure S4, Supporting Information) onto silicon wafers and analyzing them using Raman, SEM, AFM and TEM as described in Section 2.2. Table S1, Supporting Information, details the experiments and conditions conducted in the study, where the samples are referred to as G-CNCC-T-S-R-A-C, where T is the pyrolysis temperature of the biochar, S is the speed (RPM), R is the RT (min, VFD processing time), A is the alignment direction to the Earth's magnetic field (N, E, S, or W), and C is the rotation direction looking out of the tube (clockwise, CW, or counterclockwise, CCW).

3. Results and Discussion

3.1. NCC Pyrolysis and CNCC Characterization

3.1.1. Biochar Yield

Table 2 shows the yield of biochar during slow pyrolysis from 500 to 800 °C. At 500 °C, the biochar yield was 29.4 wt% and gradually decreased to 22.7 wt% as the temperature was increased to 800 °C. These results correlate well with the experiments conducted by Maiti et al.[32] who obtained biochar yields between 10 and 22 wt% during the pyrolysis of different NCCs at 800 °C. However, when compared to the pyrolysis of raw cellulose at 800 °C, yields between 5 and 7.3 wt%, which are significantly lower than the results obtained here, are often reported.[25,26] As the chemical structure of cellulose and nanocellulose are essentially the same, it was concluded that the structural difference between these materials is the reason for the differences in the observed yields for biochar.

Previous studies on cellulose pyrolysis have shown that depolymerization via glycosidic bond cleavage is the initial step during pyrolysis due to its low thermal stability (occurring from 150 to 250 °C.[33,34] This results in the formation of oligosaccharides and sugars, with levoglucosan (LVG) being one of the most abundant compounds (up to 60 wt% yield).[35] At 250–350 °C, LVG undergoes two competing pathways: evaporation (where it can then be condensed as bio-oil) or repolymerization to form biochar.[36,37] The high crystallinity of NCC results in a very compact structure, preventing the evaporation of LVG and increasing repolymerization reactions. A study by Bai et al.[38] also showed that mass transfer limitations can increase biochar yield. In their experiment, they found that as the sample of cellulose increased from 10 to 30 microliters, the repolymerization of LVG was promoted and the yield of LVG decreased from 50 to 22 mL in the condensed bio-oil. As an initial mass of 9.0 g was used in this experiment, it is likely that vapor diffusion within the biomass was also limited, enhancing biochar yields.

3.1.2. Elemental Analysis

The elemental analysis showed that as the temperature increased from 500 to 600 °C, there was a relatively large increase in carbon content and a decrease in both hydrogen and oxygen content (Table 2). This closely matches results from previous reports on biomass pyrolysis and highlights how increasing temperatures above 500 °C promotes the volatilization of oxygenated compounds, leaving a carbon-rich solid residue.[25] At 700–800 °C, the carbon and oxygen content remain stable with a slight decrease in hydrogen wt%. At these temperatures, dehydrogenation and aromatization (fusion of aromatic rings) are the main reactions that occur,[24] resulting in H_2 evolution and an observed decrease in hydrogen content (Table 2). A sulfur content of 1.47–1.75 wt% is also observed in each biochar sample which is a result of the production process of NCCs. During isolation, sulfuric acid (H_2SO_4) is employed resulting in sulfate groups (SO_4) attaching to the biomass surface,[39] which is further confirmed by FT-IR analysis.

3.1.3. FT-IR and XRD Analysis

Figure 2a compares the FT-IR spectra for NCC and the CNCC obtained at each pyrolysis temperature. The FT-IR spectrum of the NCC matches the structure of cellulose, with clear O-H stretching at 3200–3500 cm^{-1} and O—H bending at 1310 cm^{-1} confirming the presence of hydroxyl groups[40] and a strong peak at 750 cm^{-1} from C—O vibrations indicating the high presence of glycosidic bonds.[35] During pyrolysis, the structure of the NCC changes significantly, and the FT-IR spectra of the CNCC at 500 and 600 °C shows the loss of O—H and C—O peaks at 3333 cm^{-1} and 1030 cm^{-1} respectively, indicating the complete destruction of the nanocellulose structure. Stretching of C═C bonds at 1574 cm^{-1}, aromatic C—H bending from 740 to 864 cm^{-1} and C—O stretching from phenols (1118 cm^{-1}) also show the

Table 2. Carbonized nanocellulose (CNCC) yields and elemental analysis during slow pyrolysis at temperatures 500–800 °C at a heating rate of 5 °C min^{-1}, RT of 60 mins, and under 50 mL N_2 min^{-1}.

Temperature [°C][a)]	Yield [wt%]	C [wt%]	H [wt%]	O [wt%]	S [wt%]
500	29.4 ± 0.5	77.4 ± 0.2	3.33 ± 0.02	11.03 ± 0.42	1.47 ± 0.03
600	26.5 ± 0.4	83.6 ± 0.2	2.62 ± 0.04	6.09 ± 0.06	1.71 ± 0.01
700	24.6 ± 0.1	83.3 ± 0.5	2.05 ± 0.01	5.45 ± 0.02	1.65 ± 0.08
800	22.7 ± 0.2	82.1 ± 1.3	1.89 ± 0.03	6.27 ± 0.36	1.75 ± 0.06

[a)]No nitrogen detected in the biochar samples.

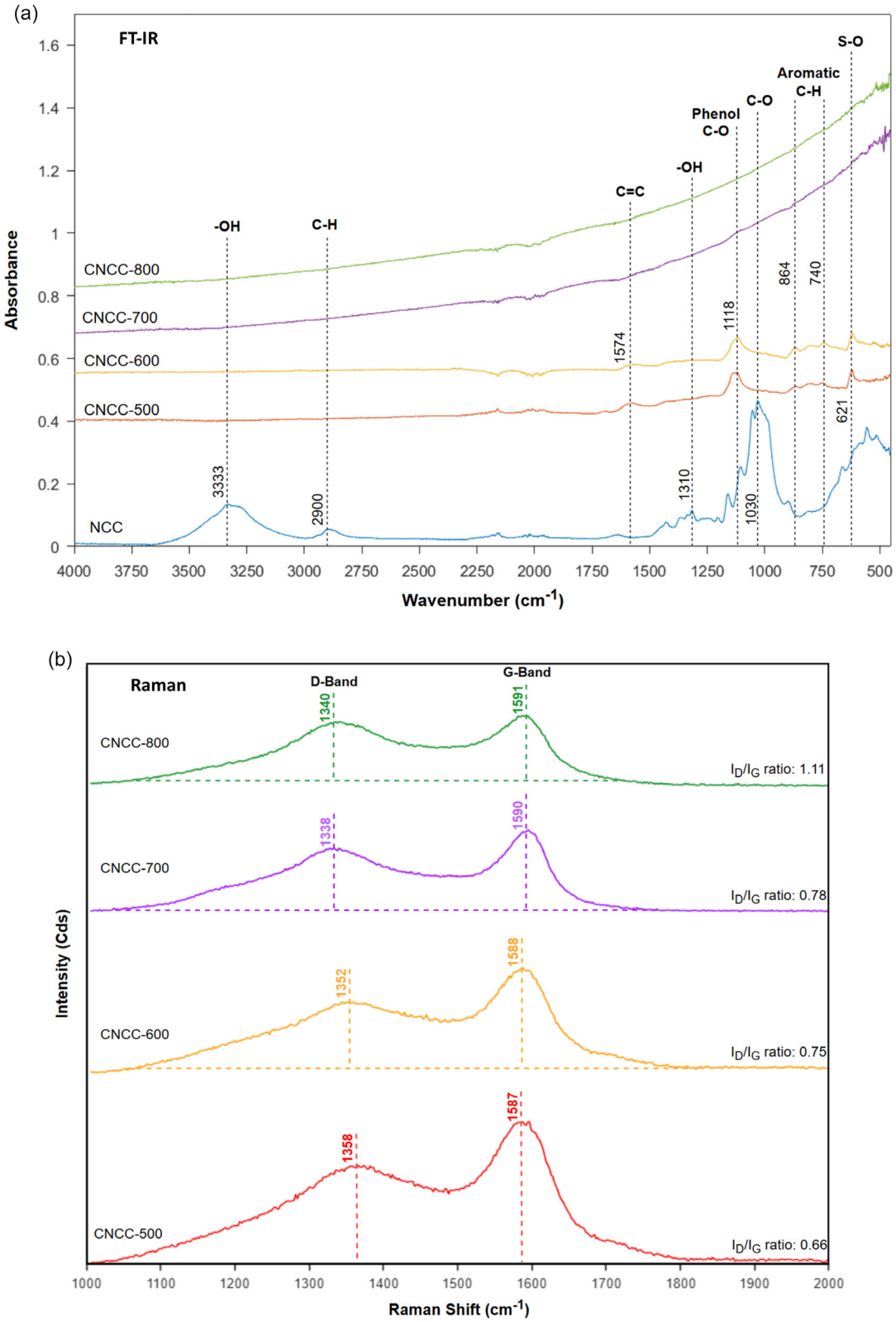

Figure 2. a) FT-IR spectra of the raw NCC and carbonized nanocellulose samples (CNCC-X). b) Raman spectra of the CNCC samples, with peak deconvolution shown in Figure S15 and S16, Supporting Information. CNCC-X samples were obtained after slow pyrolysis (5 °C min^{-1}, 60 mins, 50 mL N_2 min^{-1} at 500–800 °C), where "X" indicates the maximum pyrolysis temperature.

formation of aromatic structures at these temperatures.[41,42] Moreover, S—O bending at 621 cm^{-1} is also observed for CNCC-500 and CNCC-600 which was confirmed by XRD analysis to be due to the presence of Na_2SO_4 (Figure S1, Supporting Information).[43,44] At pyrolysis temperatures between 700 and 800 °C, no major peaks were observed in the FT-IR spectra, which is consistent with the biochar forming a condensed aromatic graphite-like structure.[40]

Interestingly, although elemental analysis of the biochar samples shows relatively high sulfur contents for CNCC-700 and 800 (Table 2), FT-IR was unable to detect the S—O bond for these samples (Figure 2a). Given that XRD was also devoid of Na_2SO_4 peaks (Figure S1, Supporting Information), it is likely that at these temperatures, Na_2SO_4 underwent decomposition and transformed into a sulfur metal, forming a carbon–sulfur–metal (C—S—M) bond.[45] A similar phenomenon was also observed during the pyrolysis of lignite, where pyrite (FeS_2) degraded >700 °C and was undetected at these temperatures by XRD.[46]

3.1.4. Raman Analysis

Figure 2b shows the Raman spectra of the CNCC samples with peaks around 1350 cm^{-1} (related to the presence of defects and structural disorder and known as the D-band) and 1590 cm^{-1} (related to the presence of crystalline graphite and known as the G-band) being typical of carbon materials. The ratio of the D and G-band intensities is known as the I_D/I_G ratio and is used to measure the crystallinity of the carbon, with lower values indicating lower amounts of defects in the carbon structure.[11] For CNCC-500, the I_D/I_G ratio was the lowest at 0.66 and gradually increased with pyrolysis temperature to a maximum of 1.11 for CNCC-800. The gradual red shift of the D band (1358 to 1340 cm^{-1}) and blue shift of the G band (1587 to 1591 cm^{-1}) is also correlated with an increase in defect degree,[47] which indicates that at higher temperatures, more defects are introduced due to the high removal of volatile matter concomitant with the growth of misoriented graphitic layers. When compared to the Raman data for raw cellulose-derived biochar however, significantly higher I_D/I_G ratios (often 1,1-2.4) are documented.[25,48,49] This shows that the removal of the amorphous region of raw cellulose results in a more suitable feedstock for the production of biochar, with better ordering of graphitic layers as well as higher yields during pyrolysis.

3.1.5. SEM

Figure 3 shows the SEM images of the NCC and CNCC samples. The NCCs display a spiral-like structure with an average particle size of 10–20 microns and a relatively smooth surface with no visible pores. After pyrolysis, the structure of the solid remains the same but the surface morphology having undergone significant changes. At 500 °C, the SEM image (Figure 3c) shows the presence of some pores and small white nanoparticles (< 100 nm), which were confirmed by EDS to be Na_2SO_4 particles (Figure S5, Supporting Information), which matches the results from FT-IR (Figure 2a) and XRD (Figure S1, Supporting Information). The biochar obtained at 600 °C exhibits

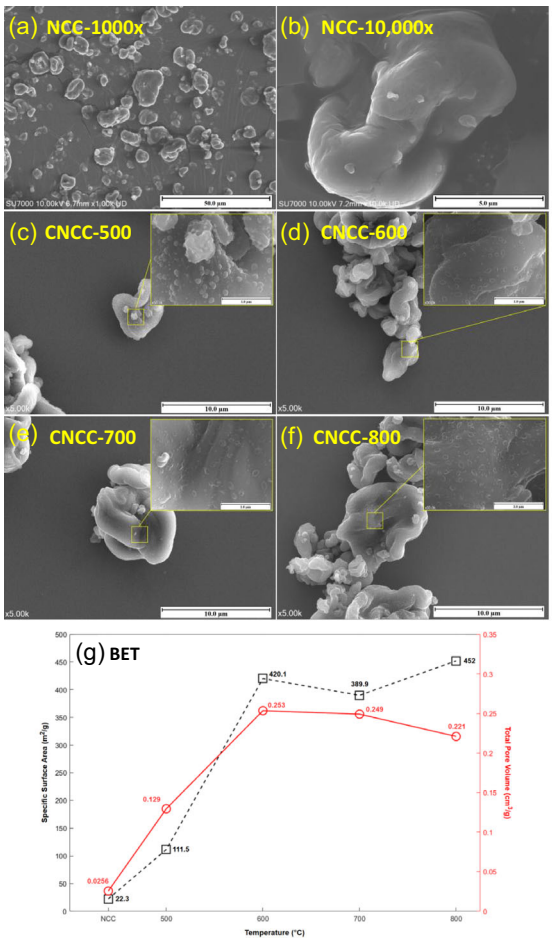

Figure 3. SEM images of the raw NCC and carbonized nanocellulose samples (CNCC-X) where the yellow squares show the images at 50,000x magnification: a,b) raw NCCs, c) CNCC-500, d) CNCC-600, e) CNCC-700, f) CNCC-800, and g) BET analysis of the NCC and CNCCs. The CNCCs were obtained after slow pyrolysis (5 °C min, 60 mins, 50 mL N_2 min^{-1} at 500–800 °C), where "X" indicates the maximum pyrolysis temperature.

a similar structure, with an abundance of large pores and cavities (30–100 nm) on the surface, which were most likely a result of aerosols forming during pyrolysis (described in 3.1.6). The Na_2SO_4 particles however are in much lower quantity at 700 and 800 °C. At 800 °C, an abundance of mesopores (2–50 nm) are observed (and confirmed from BET analysis in Figure S6, Supporting Information) which are most likely a result of physical activation (due to the presence of CO_2 and water vapor).[50,51]

3.1.6. BET and TGA

Figure 3g shows the SSA and total pore volume of the original NCC and biochar samples at each pyrolysis temperature. The original NCCs had a relatively low SSA and pore volume of 22.3 $m^2 g^{-1}$ and 0.0256 $cm^3 g^{-1}$, respectively, which was due to its flat surface and nonporous structure (Figure 3a–b). The SSA rapidly increased from 111.5 to 420.1 $m^2 g^{-1}$ as the

temperature increased from 500 to 600 °C and indicates that a minimum of 600 °C is required for the production of high-quality char from NCC. At 700 °C however, the SSA and total pore volume decreases to 389.9 $m^2 g^{-1}$ and 0.249 $cm^3 g^{-1}$, respectively. At this temperature, the widening and fusion of existing pores often occurs, resulting in a loss of SSA.[52] A comparison of the pore size distribution curves at 600 and 700 °C (Figure S6b and c, Supporting Information) confirms this and also explains why a loss of total pore volume is observed, as macropores (which can form from pore widening) cannot be measured by the BET adsorption method.[30] At 800 °C, the SSA increases again and reaches a maximum of 452 $m^2 g^{-1}$; however, the total pore volume decreases to 0.221 $cm^3 g^{-1}$. This indicates that a combination of physical activation (generating new pores (Figure 3f) and increasing the SSA) and pore widening (resulting in a decrease in pore volume) are occurring.[50,51]

Figure S7, Supporting Information, shows the thermogravimetric curve of the NCC during pyrolysis from 30 to 1000 °C. An initial weight loss of 5.8 wt% occurs <120 °C due to the evaporation of moisture in the sample. Between 150 and 250 °C, the cellulose undergoes depolymerization (with minimal mass loss) via glycosidic bond cleavage to form liquid compounds comprised of oligosaccharides, LVG, and other sugars, as shown in **Figure 4**.[53] From 250 to 320 °C, an abrupt weight loss is observed (–50.23 wt%, Figure S7, Supporting Information) due to the rapid evaporation of these compounds and formation of aerosols. However, due to the crystalline structure of NCC, evaporation is greatly reduced, and the majority of sugars (such as LVG) remain in the condensed phase where repolymerization reactions are promoted, resulting in higher char yields, as mentioned in Section 3.1.1. At 320–400 °C, a gradual mass loss is also observed (Figure S7, Supporting Information) which correlates with previous TGAs on NCC[52,54] and is most likely due to the slow release of trapped volatiles (such as acetic acid and hydroxyacetaldehyde) that were previously formed from the cracking of compounds in the vapor phase (Figure 4.[36]). As the temperature increases from 500 to 800 °C, there is a gradual reduction in mass from biochar structure rearrangement and fusion of aromatic rings (aromatization), resulting in H_2, CO_2, and water vapor evolution.[55]

3.2. Conversion of Biochar to Graphene

The CNCC obtained from pyrolysis was transformed into graphene (denoted as G-CNCC) using the VFD under different conditions (Table S1, Supporting Information). This section describes the optimization of the VFD processing conditions

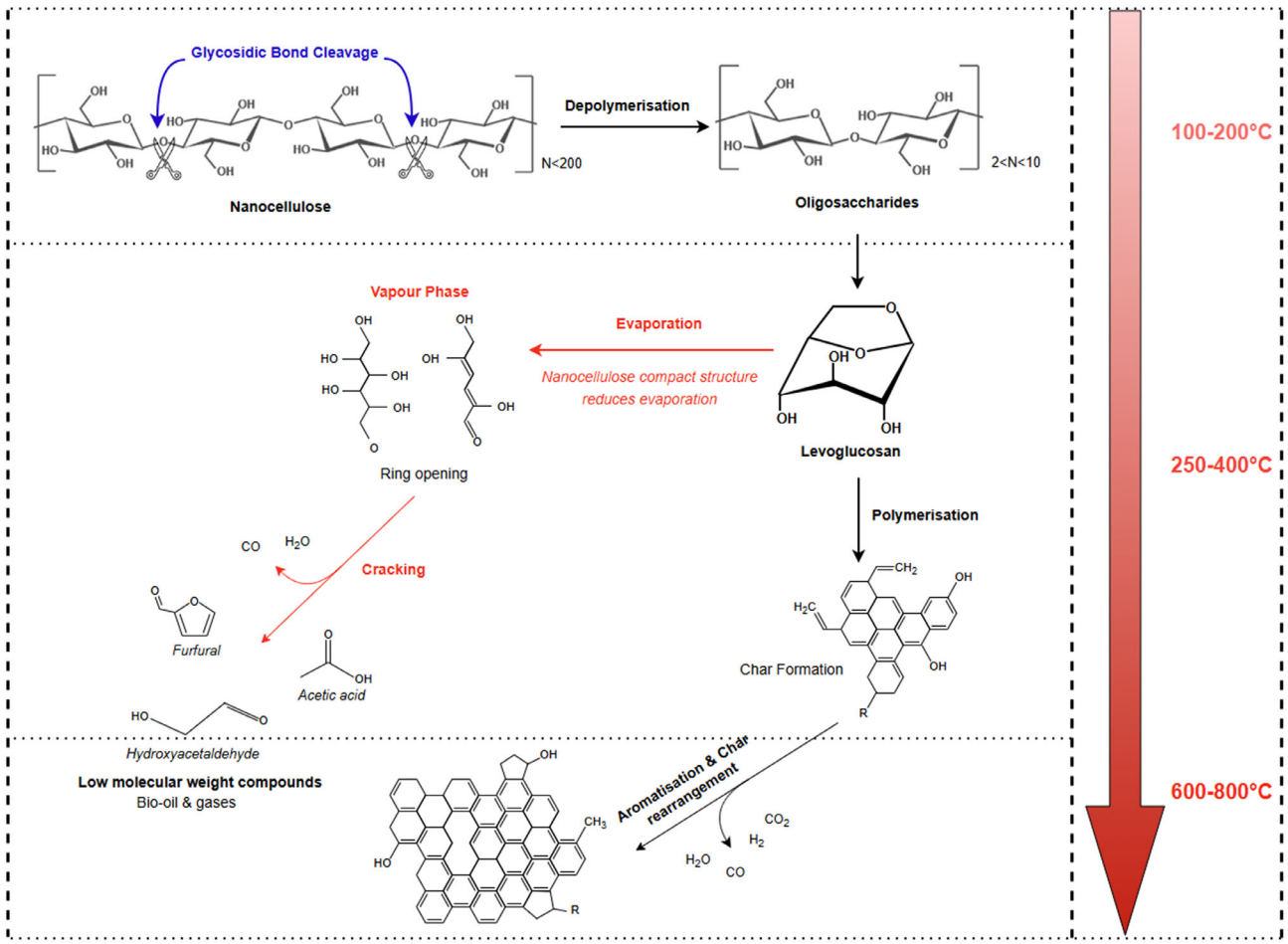

Figure 4. Overall mechanism for the pyrolysis of nanocellulose (adapted from ref. [55]).

and their impact on the final product, which includes the pyrolysis temperature for generating the CNCC, the RPM, RT, and magnetic field alignment. The initial feedstock was CNCC-600 and initial conditions prior to optimization were 7000 rpm, 30 min under clockwise (CW) rotation (looking out of the tube) in the south direction (with respect to Earth's magnetic field) based on previous studies on graphite exfoliation.[17,18] The initial magnetic field direction (south) and pyrolysis temperature (CNCC-600) were chosen based on preliminary tests. The samples are referred to as G-CNCC-T-S-R-A-C, where T is the pyrolysis temperature of the biochar, S is the speed (RPM), R is the RT (min), A is the alignment direction to the Earth's magnetic field (N, NW, E, S, SE, or W), and C is the rotation direction looking out of the tube (clockwise, CW, or counterclockwise, CCW).

3.2.1. Impact of RT and RPM

The impact of processing time in the VFD was investigated at 7000 rpm in the south-CW direction, and after 15–30 min, there was no change in the morphology of the particles when compared to the original CNCC-600 (Figure S8a-b, Supporting Information). **Figure 5**a shows that after 60 min, there was some evidence of graphene formation, and extending the RT to 120 min resulted in the transformation of the spiral structures into large sheets, with smaller sheet fragments (1–2 microns) also present (Figure 5c–d). The impact of RPM at 5000 (Figure 5e) and 8500 rpm (Figure 5f) at 60 min was also investigated. The particle morphology remained the same at 5000 rpm, while 8500 resulted in the formation of graphene, indicating that a high RPM (>7000) is desirable for forming graphene in the VFD. However, the impact of RT was overall much more significant than an increase in the RPM. A higher RPM also increases power usage; therefore, an optimal RPM and RT was concluded to be 7000 and 120 mins, respectively.

3.2.2. Impact of Biochar Properties

Figure 5g–h compares SEM images of the G-CNCC at 600 and 800 °C after processing in the VFD at the optimized RPM (7000) and RT (120 mins) in the south-CW direction. For G-CNCC-500 and 700 (Figure S8k–L, Supporting Information), the particles show very little changes after processing in the VFD, while for G-CNCC-800, small levels of "unravelling" occurred, similar to the morphology shown after 60 mins for G-CNCC-600 (Figure 5b). Interestingly though, G-CNCC-600 exhibited a significant amount of thin 2D material (Figure 5g) when compared to the other biochar samples. A possible reason for low exfoliation at higher temperatures could be due to the formation of carbon-sulfur crosslinks that occurred during the decomposition of Na_2SO_4. These highly stable bonds could hold aromatic layers in place and hinder the exfoliation process, though due to the low concentration of sulfur, it is unlikely that this was the sole reason for the differences observed. FT-IR (Figure 2a) indicate that CNCC-600 contained high amounts of functional groups, while CNCC-800 was composed of a condensed aromatic structure. The Raman analysis (Figure 2b) also shows that CNCC-600 contained a relatively low defect degree (I_D/I_G ratio of 0.75) when compared to CNCC-800 (I_D/I_G ratio of 1.11), which is supported

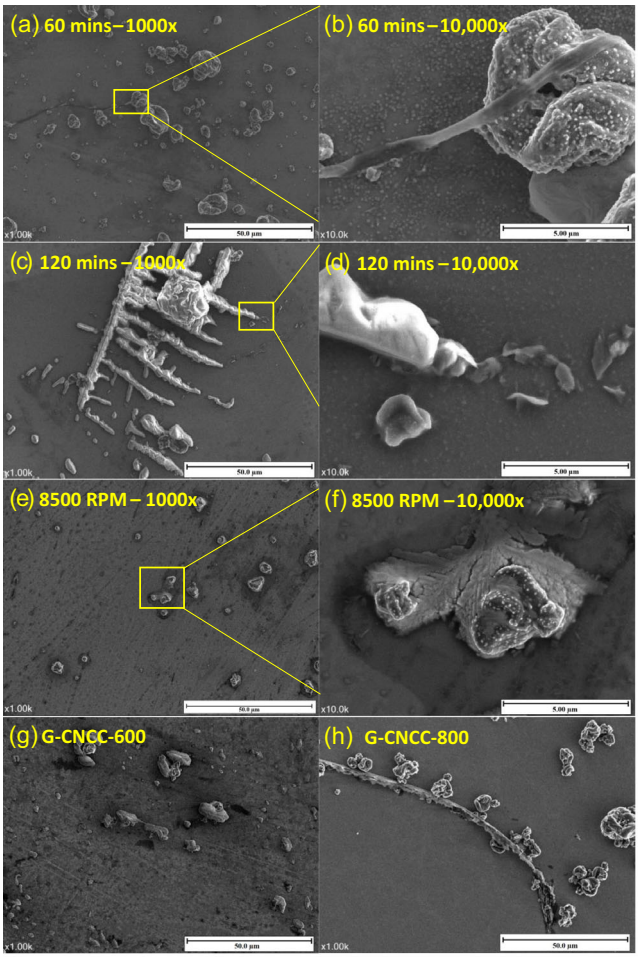

Figure 5. SEM imaging of carbonized nanocellulose-derived graphene (G-CNCC) samples obtained after different VFD processing times, RPMs, and temperatures: a) 60 mins, 1000x (G-CNCC-600-7000-60-S-CW); b) 60 mins, 10,000x (G-CNCC-600-7000-60-S-CW); c) 120 mins, 1000x (G-CNCC-600-7000-120-S-CW); d) 120 mins, 10,000x (G-CNCC-600-7000-120-S-CW); e,f) 8500 rpm after 60 mins (CNCC-600-8500-60-S-CW); g) G-CNCC-600, 1000x; h) G-CNCC-800, 1000x.

by the XRD results (Figure S1, Supporting Information). It was therefore proposed that the presence of functional groups and low defect density can also assist with the exfoliation to form G-CNCC.

However, as G-CNCC-500 did not result in the formation of graphene despite similar FT-IR, another property of the biochar must also play a key role. The BET analysis (Figure 3g) showed that the SSA of CNCC-600 (420.1 $m^2 g^{-1}$) was significantly higher than CNCC-500 (111.5 $m^2 g^{-1}$) which could explain the difference in graphene formation. As such, it was concluded that 600 °C was the optimal pyrolysis temperature due to the high SSA and presence of functional groups. A similar observation was also made by Yan et al.[56] who found that from 800 to 1500 °C, 1200 °C was the most optimal pyrolysis temperature for biochar exfoliation as the interlayer spacing (due to the presence of functional groups) was the highest (0.449 nm). HR-TEM imaging shows that in this study, CNCC-600 also had the highest

interlayer spacing (0.39 nm) when compared to CNCC-700 (0.34 nm) and CNCC-800 (0.33 nm, Figure S9a–d, Supporting Information). As a higher interlayer distance helps reduce the dispersion forces between layers while high SSA increases fluid contact resulting in greater shear forces, it is clear that these properties are pivotal for the conversion of biochar to graphene.

3.2.3. Impact of the Earth's Magnetic Field

At the optimized RPM (7000), RT (120 mins), and pyrolysis temperature (600 °C), the impact of the Earth's magnetic field on the CNCC conversion to graphene (G-CNCC) was first investigated by changing the VFD alignment to north, east, south, and west and rotating in both clockwise (CW) and counterclockwise (CCW) directions. This study followed our recent finding on the ability to twist toroids of self-assembled single walled carbon nanotubes (SWCNTs) into left handed or righted handed figure of 8s (lemniscates) by simply changing the rotation of the tube from CW to CCW and vice versa, in a way that is dependent of the orientation of the VFD tube relative to the Earth's magnetic field and the geographical location of the VFD.[57] **Figure 6** shows that south-CW and north-CCW processing were the most optimal for graphene production and resulted in the formation of few-layered graphene. Furthermore, north-CW, south-CCW, and east and west (both CW and CCW) processing showed no changes in morphology (Figure S8c–h, Supporting Information).

The impact of the Earth's magnetic field on fluid exfoliation has not been reported, and though the following section attempts to describe the observations that occurred in this experiment, it should be noted that this is a working hypothesis that requires further validation. It is a well-known phenomenon that contact electrification (CE) occurs during water-solid contact and has occurred in the VFD in other experiments[58,59]). CE between water and biochar would most likely occur at the biochar-liquid interface due to the high shear flows that occurs in the spinning top (ST) topological fluid flows.[60] These ST flows are estimated to have pressures of 20 MPa[57] and can generate temperatures at least as high as 630 °C.[16] Such forcing conditions are similar to the metamorphic processes that occur for natural graphite formation and are therefore likely to transform the biochar into graphite which then undergoes exfoliation (Figure 6i).

During CE, the fluid becomes charged and is subjected to a Lorentz force due to the Earth's magnetic field. **Figure 7** shows that in the south-CW direction, the ST flows almost perpendicular to the Earth's magnetic field (at James Cook University, Townsville) resulting in the Lorentz force to push the ST flow outwards, increasing the area of graphite formation and subsequent exfoliation. This also indicates that the ST flow during CE becomes negatively charged given that processing in the south-CCW direction (where the Lorentz force now acts towards the center of the ST flow, Figure S10b, Supporting Information) did not afford graphene. This, however, does not explain why graphene was observed in the north-CCW direction (Figure 6a–e) but not for west or east (CW and CCW) as the Lorentz force in these orientations act on the ST flow in similar directions (Figure S10c–d, Supporting Information). If CE occurs at the ST-biochar interface due to the high pressure and mass transfer in this region, it is reasonable to assume that

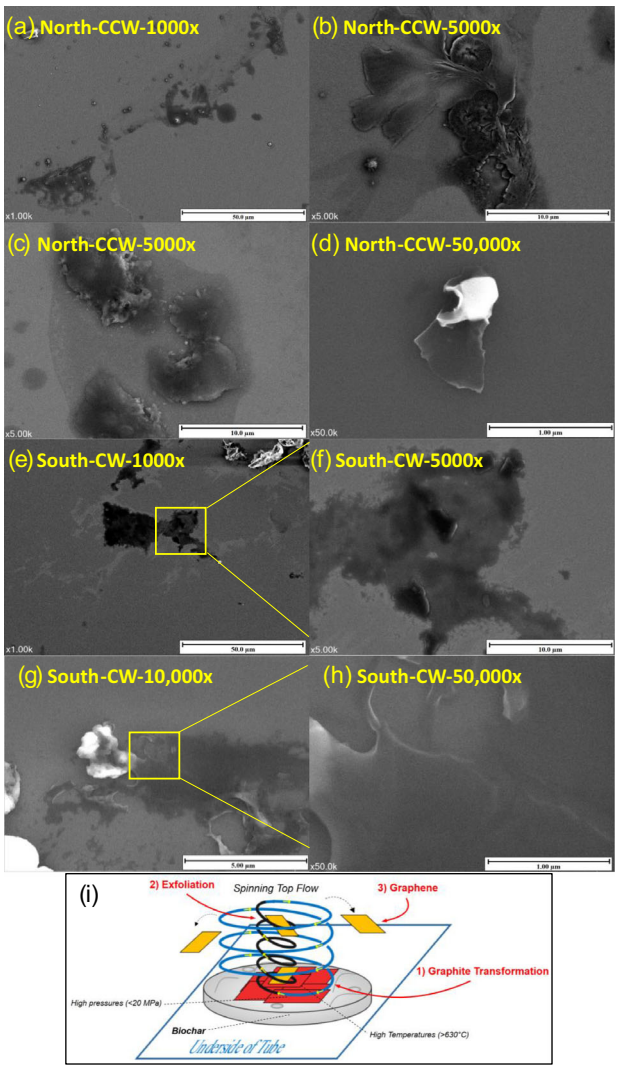

Figure 6. a–h) SEM images for VFD processing CNCC-600 at 7000 rpm for 120 min in the (a–d) north-CCW direction (G-CNCC-600-7000-120-N-CCW) and (e–h) south-CW direction (G-CNCC-600-7000-120-S-CW); i) transformation of biochar to graphite and subsequent exfoliation at the base of the tube where pressures and temperatures of 20 MPa and at least as high as 630 °C, respectively, are present due to the formation of the ST topological fluid flows (adapted from ref. [64]).

a Lorentz force also acts on the charged biochar particles as it rotates around the tube.

In the east and west directions (Figure S10c–d, Supporting Information), there is no net Lorentz force on the biochar as it acts in both directions along the tube, while in the north direction (CCW), the Lorentz force acts on the biochar towards the center (Figure S10a, Supporting Information). It is proposed that when the Lorentz force acts towards the center of the tube, it pulls the surface layer apart vertically, reducing the dispersion forces and allowing the layer to slip under the shear stresses more easily; whereas when it acts towards the outside (during north-CW processing), it does not promote exfoliation. Graphene exfoliation models show that "peeling" of graphene

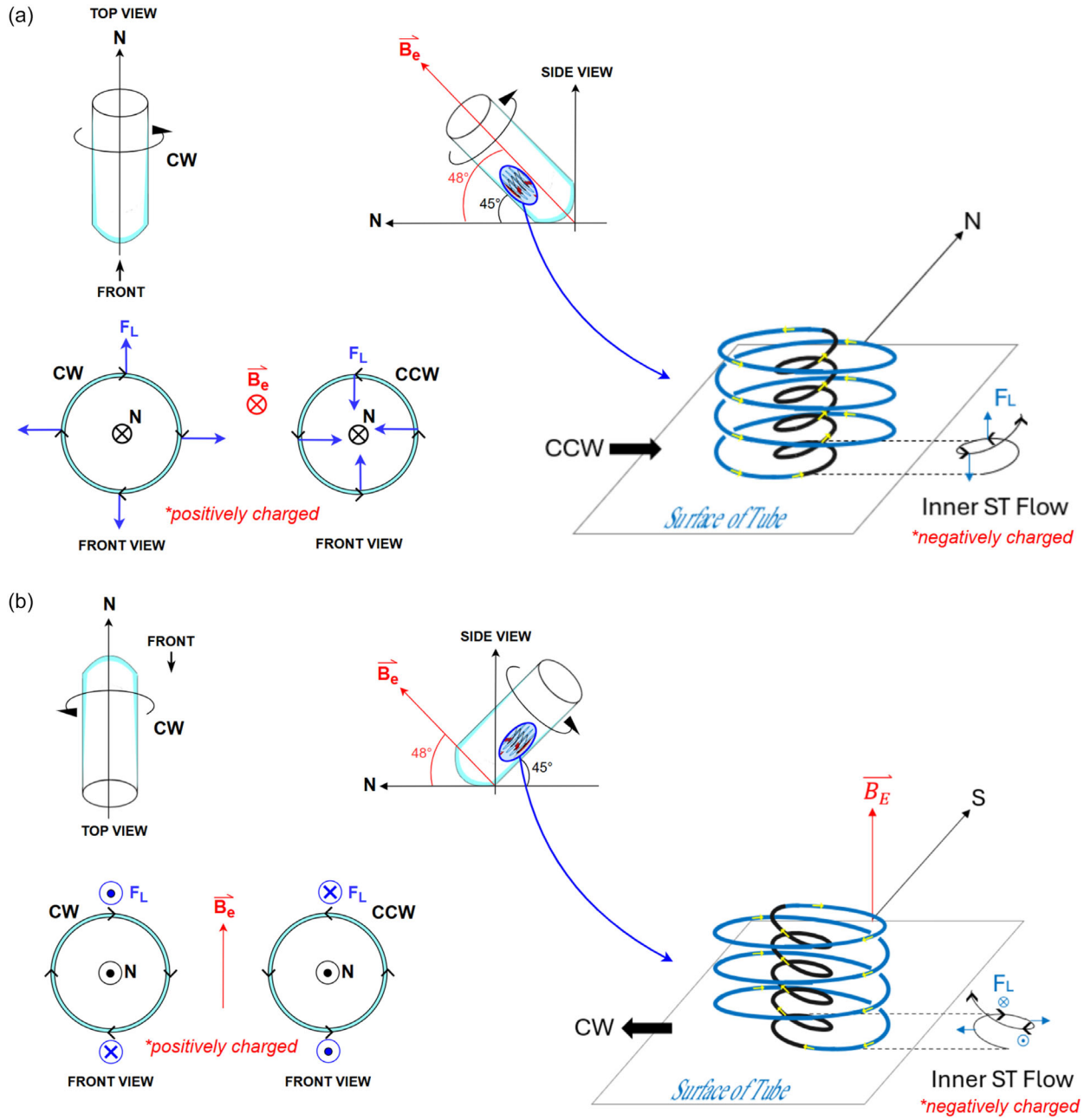

Figure 7. Direction of the Lorentz force acting on the positively charged biochar rotating around the tube in the CW and CCW rotation and on the negatively charged ST flow when the VFD is aligned in the a) north direction and b) south direction. The magnetic field inclination (−48°) and magnitude (48.9 μT) at Townsville, James Cook University, was taken from the National Oceanic and Atmospheric Administration[65] in November 2024–February 2025 when the experiments were conducted (Figure S11, Supporting Information).

layers is energetically favored over purely normal or shearing exfoliation[61] and that "pulling" forces acting perpendicular to graphene increase the ability for solvents to intercalate between the layers and assist with exfoliation.[62] In the north-CCW direction, at 7000 rpm, with a magnetic field of 49 μT at James Cook University (where the experiments were conducted), the magnitude of the Lorentz force acting on the biochar was determined to be 314q μN, where q is the charge (Figure S12, Supporting Information). This may further explain why a high SSA is desirable for exfoliation (as mentioned in Section 3.2.2), as increased water-solid contact can result in higher CE and greater charges, resulting in higher Lorentz forces. As previous studies have shown that forces perpendicular to graphene layers as small as 0.16 μN is enough for exfoliation to occur,[62] these results indicate how electric fields can affect exfoliation, though further studies are needed to validate this mechanism. In summary, this

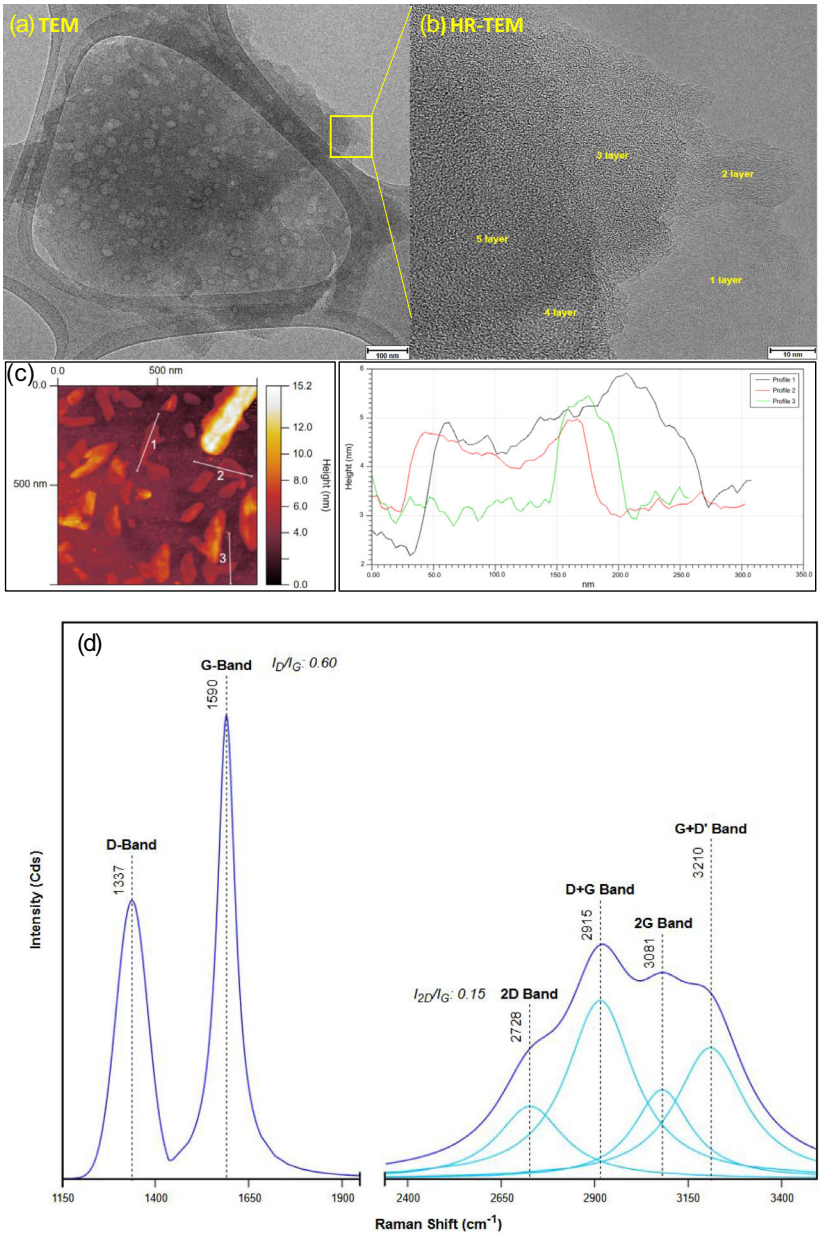

Figure 8. Characterization of the graphene obtained after VFD processing of CNCC-600 at the optimal conditions (7000 rpm for 120 min counterclockwise in the north direction, G-CNCC-600-7000-120-N-CCW): a) TEM, b) HR-TEM, c) AFM analysis with right graph depicting the height profile of the selected areas, and d) Raman spectra with I_D/I_G and I_{2D} /I_G ratios determined from peak deconvolution shown in Figure S15, Supporting Information.

study showed that the Earth's magnetic field significantly impacts on both the fluid flow (as shown in south-CW processing) and exfoliation process (as shown in N-CCW processing) in the VFD.

3.3. Graphene Yield and Characterization

At the optimized conditions for graphene production (CNCC-600 feedstock processed in the VFD at 7000 rpm, 120 min in the north direction and counterclockwise rotation), the absorbance at 660 nm was 0.043 (Figure S13, Supporting Information) and estimated using UV-VIS spectroscopy to equate to a yield of 2.8 wt% (Equation (2)). An energy analysis shows that this yield would result in an energy consumption of 28 980 MJ kg^{-1} graphene for this process (see supplementary information). Although this energy cost is significantly higher than CVD and ultrasonication, these methods are known for inherently being unscalable synthesis routes, and when compared to the other scalable methods, chemical oxidation-reduction and ball milling, the energy cost is lower (Table 1). This highlights the potential for this process to be a low-cost, scalable, and sustainable synthesis route, with further studies looking to increase the

yield and lower the required speed and processing times of exfoliation to further reduce energy costs.

Figure 8a shows the TEM obtained for the graphene obtained at the optimal processing conditions (north-CCW, 7000 rpm and 120 min processing) in the VFD. The material exhibited multiple pores, presumably from the Na_2SO_4 particles which were removed during exfoliation. TEM shows the presence of monolayer graphene gradually stacking individually up to 5 layers (Figure 8b). AFM analysis (Figure 8c) shows that graphene platelets were ≈2–3 nm on average in height, though flakes as small as 1 nm height were also observed (Figure S14, Supporting Information). With an interlayer spacing of 0.39 nm (Figure S9, Supporting Information), this results in ≈3–8 layered graphene, which matches the TEM analysis and further confirming successful exfoliation.

Raman spectra of the G-CNCC (Figure 8d) shows peaks at 1338 cm^{-1}, 1590 cm^{-1}, and 2738 cm^{-1} and are commonly known as the D-band, G-band, and 2D-band, respectively. The intensity ratio of the 2D and G peaks is known as the I_{2D} /I_G ratio and was determined to be 0.15, indicating that the material is predominantly composed of few-layered graphene[63] and correlating with the results from AFM and TEM. The presence of other overtone bands alongside the 2D band also indicates the presence of oxygenated functional groups, similar to GO and rGO, and is likely from the retention of the functional groups present in the original CNCC-600.

The intensity ratio of the D and G band (known as the I_D/I_G ratio) is a measure of graphene quality, with lower values translating to a lower number of defects. In our study, the I_D/I_G ratio of the G-CNCC was determined to be 0.60 which is lower than the feed value of the original CNCC-600 (I_D/I_G ratio = 0.75, Figure 2b), similar to the values obtained from other exfoliation studies (between 0.1 and 0.8) using graphite as feedstock and much lower than previous values obtained for biochar-derived graphene (I_D/I_G ratio <1, Table S2, Supporting Information). It has been shown that exfoliation often introduces more defects due to increased presence of edge defects[6] resulting in higher I_D/I_G ratio values. However, in this case, the relative degree of defects was reduced after VFD processing, providing further evidence of the biochar-to-graphite transformation process described in Section 3.2.3.[37,49–34]

4. Conclusions

This study aimed to investigate a scalable, low-cost, and sustainable method of graphene synthesis using pyrolysis and fluid mediated conversion of biochar to graphene in the VFD. NCCs were converted into biochar at 500–800 °C under slow pyrolysis conditions and transformed into graphene in water using the VFD. The pyrolysis of nanocellulose at 600 °C yielded 26.5 wt% biochar, which exhibited an SSA of 420.1 $m^2 g^{-1}$ with FT-IR confirming the presence of both phenol and aromatic functional groups. The biochar produced at 600 °C showed high degrees of graphene formation in the VFD when compared to the other biochar temperatures (500, 700, and 800 °C), and it was proposed that the high SSA resulted in increased shear forces and CE, while the presence of functional groups increased the interlayer distance, reducing dispersion forces and easing the exfoliation process. The impact of the VFD's orientation with respect to the Earth's magnetic field was also investigated, and it was shown that the direction of the Lorentz force played a significant role in the formation of graphene. The biochar-derived graphene exhibited relatively high quality with Raman showing an I_D/I_G ratio of 0.60 and an I_{2D}/I_G ratio of 0.15, with TEM and AFM identifying the presence of 3–8 layers. In summary, this was the first study that explored a scalable, catalyst-free, and low-energy method of converting biochar into graphene. Further studies on the graphene application, impact of biochar morphology, and use of more widely available biomass such as wood and agricultural wastes still need to be investigated, along with the use of applied magnetic fields instead of the relatively weak Earth's magnetic field to improve the transformation process and increase the final quality of the graphene.

Supporting Information

Supporting Information is available from the Wiley Online Library or from the author.

Acknowledgements

The authors would like to greatly acknowledge Dr. Sara Miller (Flinders University, Adelaide) for her assistance with conducting the Raman spectroscopy analysis. The authors would also like to acknowledge the "James Cook University Australia Research Training Program" scholarship for funding this research.

Conflict of Interest

The authors declare no conflict of interest.

Author Contributions

Yu Matsueda: conceptualization (equal); data curation (lead); formal analysis (equal); investigation (equal); methodology (equal); validation (lead); visualization (lead); writing—original draft (lead); writing—review and editing (equal). **Colin L. Raston**: formal analysis (supporting); writing—review and editing (supporting). **Elsa Antunes**: conceptualization (equal); formal analysis (equal); funding acquisition (lead); investigation (equal); methodology (equal); resources (lead); supervision (lead); writing—review and editing (supporting).

Data Availability Statement

The data that support the findings of this study are available from the corresponding author upon reasonable request.

Keywords

biochar, fluid exfoliations, graphene, nanocellulose, pyrolysis, sustainable

Received: August 10, 2025
Revised: September 30, 2025
Published online:

[1] M. A. A. Farid, Y. Andou, *J. Cleaner Prod.* **2022**, *380*, 135090.
[2] F. Zhang, K. Yang, G. Liu, Y. Chen, M. Wang, S. Li, R. Li, *Comp. Part A Appl. Sci. Manuf.* **2022**, *160*, 107051.
[3] M. Davis **2020**, Now, scientists can make it from trash. Bigthink.com. Accessed on August 10, 2025, https://bigthink.com/the-present/flash-graphene/.
[4] J. K. Saha, A. Dutta, *Waste Biomass Valor.* **2022**, *13*, 1385.
[5] E. Varrla, K. R. Paton, C. Backes, A. Harvey, R. J. Smith, J. McCauley, J. N. Coleman, *Nanoscale* **2014**, *6*, 11810.
[6] Y. Arao, Y. Mizuno, K. Araki, M. Kubouchi, *Carbon* **2016**, *102*, 330.
[7] F. Chen, J. Yang, T. Bai, B. Long, X. Zhou, *J. Electroanal. Chem.* **2016**, *768*, 18.
[8] Y. Zhou, J. He, R. Chen, X. Li, *Mater. Today Sustainability* **2022**, *18*, 100138.
[9] M. Yi, Z. Shen, *J. Mater. Chem. A* **2022**, *3*, 11700.
[10] M. T. U. Safian, U. S. Haron, M. M. Ibrahim, *BioResources* **2020**, *15*, 9756.
[11] K. R. Paton, E. Varrla, C. Backes, R. J. Smith, U. Khan, A. O'Neill, J. N. Coleman, *Nat. Mater.* **2014**, *13*, 624.
[12] J. Stafford, A. Patapas, N. Uzo, O. K. Matar, C. Petit, *AIChE J.* **2018**, *64*, 3246.
[13] P. G. Karagiannidis, S. A. Hodge, L. Lombardi, F. Tomarchio, N. Decorde, S. Milana, A. C. Ferrari, *ACS Nano* **2017**, *11*, 2742.
[14] N. Blomquist, A. C. Engström, M. Hummelgård, B. Andres, S. Forsberg, H. Olin, *PloS one* **2016**, *11*, e0154686.
[15] K. Vimalanathan, C. L. Raston, *Adv. Mater. Technol.* **2017**, *2*, 1600298.
[16] F. A. Alrashaidi, S. Rahpeima, X. Luo, K. Vimalanathan, A. S. Alotabi, T. Alharbi, C. L. Raston, *RSC Mechanochem.* **2024**, *1*, 432.
[17] X. Chen, J. F. Dobson, C. L. Raston, *Chem. Comm.* **2012**, *48*, 3703.
[18] M. H. Wahid, E. Eroglu, X. Chen, S. M. Smith, C. L. Raston, *Green Chem.* **2013**, *15*, 650.
[19] Z. Shi, S. Wang, Y. Jin, L. Zhao, S. Chen, H. Yang, T. Han, *SusMat* **2023**, *3*, 402.
[20] J. Nylen, M. Sheehan, *Energies* **2023**, *16*, 1964.
[21] H. S. Kambo, A. Dutta, *Renewable Sustainable Energy Rev.* **2015**, *45*, 359.
[22] H. You, J. Hui, Y. Zhou, K. Vittore, J. Zhang, L. E. Chaney, S. J. Rowan, *Small* **2024**, *20*, 2406669.
[23] M. C. Iglesias, D. Gomez-Maldonado, B. K. Via, Z. Jiang, M. S. Peresin, *Forest Prod. J.* **2020**, *70*, 10.
[24] M. W. Smith, G. Helms, J. S. McEwen, M. Garcia-Perez, *Carbon* **2017**, *116*, 210.
[25] C. Zhang, L. Chao, Z. Zhang, L. Zhang, Q. Li, H. Fan, X. Hu, *Renewable Sustainable Energy Rev.* **2021**, *135*, 110416.
[26] M. Fan, C. Li, Y. Shao, S. Zhang, M. Gholizadeh, X. Hu, *Sci. Total Environ.* **2022**, *825*, 153959.
[27] E. C. Sumarago, M. F. M. Dela Cerna, A. K. B. Leyson, N. P. B. Tan, K. F. Magsico, *Polymers* **2024**, *16*, 1312.
[28] K. Lichtenstein, N. Lavoine, *Polym. Degrad. Stab.* **2017**, *146*, 53.
[29] M. W. Smith, I. Dallmeyer, T. J. Johnson, C. S. Brauer, J. S. McEwen, J. F. Espinal, M. Garcia-Perez, *Carbon* **2016**, *100*, 678.
[30] L. Leng, Q. Xiong, L. Yang, H. Li, Y. Zhou, W. Zhang, H. Huang, *Sci. Total Environ.* **2021**, *763*, 144204.
[31] M. Ojrzynska, A. Wroblewska, J. Judek, A. Malolepszy, A. Duzynska, M. Zdrojek, *Opt. Express* **2020**, *28*, 7274.
[32] S. Maiti, J. Jayaramudu, K. Das, S. M. Reddy, R. Sadiku, S. S. Ray, D. Liu, *Carbohydr. Polym.* **2013**, *98*, 562.
[33] J. Lédé, *J. Anal. Appl. Pyrolysis* **2012**, *94*, 17.
[34] Y. C. Lin, J. Cho, G. A. Tompsett, P. R. Westmoreland, G. W. Huber, *J. Phys. Chem. C* **2009**, *113*, 20097.
[35] Z. Wang, B. Pecha, R. J. Westerhof, S. R. Kersten, C. Z. Li, A. G. McDonald, M. Garcia-Perez, *Ind. Eng. Chem. Res.* **2014** *53*, 2940.
[36] E. Leng, L. Yang, T. Wang, S. Du, H. Tian, S. Cheng, Y. Yu, *Fuel* **2024**, *358*, 130109.
[37] X. Bai, R. C. Brown, *J. Anal. Appl. Pyrol.* **2014**, *105*, 363.
[38] X. Bai, P. Johnston, R. C. Brown, *J. Anal. Appl. Pyrolysis* **2013**, *99*, 130.
[39] A. Q. Almashhadani, C. P. Leh, S. Y. Chan, C. Y. Lee, C. F. Goh, *Carbohydr. Polym.* **2022**, *286*, 119285.
[40] V. Ţucureanu, A. Matei, A. M. Avram, *Crit. Rev. Anal. Chem.* **2016**, *46*, 502.
[41] M. Uchimiya, A. Orlov, G. Ramakrishnan, K. Sistani, *J. Anal. Appl. Pyrolysis* **2013**, *102*, 53.
[42] Z. Ma, Y. Yang, Y. Wu, J. Xu, H. Peng, X. Liu, W. Zhang, S. Wang, *JAAP.* **2019**, *140*, 195.
[43] S. Kane, D. B. Hodge, B. Saulnier, V. E. Bécsy-Jakab, D. N. Dülger, C. Ryan, *J. Anal. Appl. Pyrolysis* **2024** *181*, 106600.
[44] Y. S. Vidya, B. N. Lakshminarasappa, *Phys. Res. Int.* **2013**, *2013*, 641631.
[45] L. Leng, R. Liu, S. Xu, B. A. Mohamed, Z. Yang, Y. Hu, H. Li, *J. Environ. Chem. Eng.* **2022**, *10*, 107185.
[46] J. Hou, Y. Ma, S. Li, J. Shi, L. He, J. Li, *Fuel* **2018**, *231*, 134.
[47] S. Keerthanan, S. M. Rajapaksha, L. Trakal, M. Vithanage, *Environ. Res.* **2020**, *189*, 109865.
[48] S. Xin, H. Yang, Y. Chen, M. Yang, L. Chen, X. Wang, H. Chen, *J. Anal. Appl. Pyrol.* **2015**, *116*, 263.
[49] Y. Eom, S. M. Son, Y. E. Kim, J. E. Lee, S. H. Hwang, H. G. Chae, *Carbon* **2019**, *150*, 142.
[50] C. O. Cope, D. S. Webster, D. A. Sabatini, *Sci. Total Environ.* **2014**, *488*, 554.
[51] J. S. Cha, S. H. Park, S. C. Jung, C. Ryu, J. K. Jeon, M. C. Shin, Y. K. Park, *J. Ind. Eng. Chem.* **2016**, *40*, 1.
[52] Y. Guo, Y. Zhang, D. Zheng, M. Li, J. Yue, *Int. J. Biol. Macromol.* **2020**, *163*, 927.
[53] J. Lédé, *JAAP.* **2012**, *94*, 17.
[54] P. Phanthong, G. Guan, Y. Ma, X. Hao, A. Abudula, *J. Taiwan Inst. Chem. Eng.* **2016**, *60*, 617.
[55] T. Yeamsuksawat, H. J. Kim, Y. Eom, *Materials Today Energy*, **2024**, *43*, 101604.
[56] Y. Yan, Y. Meng, H. Zhao, E. Lester, T. Wu, C. H. Pang, *Bioresour. Technol.* **2021**, *331*, 124934.
[57] M. Jellicoe, Z. Gardner, A. E. Alotaibi, K. E. Shoemaker, J. M. Scott, S. Wang, C. L. Raston, *Small* **2025**, *21*, 2409807.
[58] B. M. Alotaibi, Z. Gardner, K. Vimalanathan, X. Chen, T. M. D. Alharbi, C. L. Raston, *Small Science.* **2024**, *4*, Portico. https://doi.org/10.1002/smsc.202300312.
[59] D. Chen, M. Usman Zia, T. M. D. Alharbi, J. R. Harmer, C. L. Raston, Q. Li, *ChemSusChem.* **2025**, *18*, Portico. https://doi.org/10.1002/cssc.202402182.
[60] T. M. Alharbi, M. Jellicoe, X. Luo, K. Vimalanathan, I. K. Alsulami, B. S. A. Harbi, C. L. Raston, *Nanoscale Adv.* **2021**, *3*, 3064.
[61] R. C. Sinclair, J. L. Suter, P. V. Coveney, *Phys. Chem. Chem. Phys.* **2019**, *21*, 5716.
[62] L. Cai, G. Tan, X. Jing, Y. Wu, Z. Liu, *J. Mol. Liq.* **2023**, *382*, 121873.
[63] A. S. Nair, S. S. Sreejakumari, J. Venkatesan, R. B. Rakhi, R. R. Sumathi, K. Jayasankar, *Diamond Relat. Mater.* **2024**, *144*, 111025.

[64] T. M. Alharbi, C. L. Raston, *Nanoscale Adv.* **2023**, *5*, 6405.
[65] National Oceanic and Atmospheric Administration. **2024**, *Magnetic Field Calculators*. NOAA. Accessed on August 10, 2025, https://www.ngdc.noaa.gov/geomag/calculators/magcalc.shtml?#igrfwmm
[66] L. Ge, M. Zuo, Y. Wang, R. Wang, N. Rong, Z. Qi, C. Xu, *J. Anal. Appl. Pyrolysis* **2024** *177*, 106320.
[67] M. Saeed, Y. Alshammari, S. A. Majeed, E. Al-Nasrallah, *Molecules* **2020**, *25*, 3856.
[68] J. Munuera, L. Britnell, C. Santoro, R. Cuéllar-Franca, C. Casiraghi, *2D Mater.* **2021** *9*, 012002.
[69] M. T. U. Safian, K. Umar, M. N. M. Ibrahim, *J. Cleaner Prod.* **2021**, *318*, 128603.
[70] S. Bai, L. Ruan, H. Chen, Y. Du, H. Deng, N. Dai, Y. Tang, *Chem. Eng. J.* **2024**, *493*, 152805.
[71] M. G. Sumdani, M. R. Islam, A. N. A. Yahaya, S. I. Safie, *J. Nanopart. Res.* **2021** *23*, 253.
[72] M. Yi, Z. Shen, *RSC Adv.* **2016**, *6*, 72525.